THE ASTROPHYSICAL JOURNAL, 419:398–417, 1993 December 10

MAGNETOSPHERES OF SOLAR ACTIVE REGIONS INFERRED FROM SPECTRAL-POLARIZATION OBSERVATIONS WITH HIGH SPATIAL RESOLUTION

K. R. LANG, R. F. WILLSON, AND J. N. KILE
Department of Physics and Astronomy, Robinson Hall, Tufts University, Medford, MA 02155
J. LEMEN AND K. T. STRONG
Lockhead Palo Alto Research Laboratory, Dept. 91-30, Bldg. 252, 3251 Hanover Street, Palo Alto, CA 94304
V. L. BOGOD, G. B. GELFREIKH, B. I. RYABOV, AND S. R. HAFIZOV
Special Astrophysical Observatory RAS, St. Petersburg 196140, Russia
AND
V. E. ABRAMOV AND S. V. SVETKOV
Pulkovo Astronomical Observatory, St. Petersburg 196140, Russia
Received 1993 April 16; accepted 1993 June 18

ABSTRACT

The strong magnetic fields of active regions organize both the plasma structures and energy processes in the chromosphere and corona. Recent radio observations with high spatial resolution permit measurements of the magnetic fields in these regions and also localize regions of thermal and nonthermal energy release. They can additionally be used to determine temperatures and electron densities in these regions. The results of such diagnostics suggest the term *magnetosphere* for the space surrounding an active region in the solar atmosphere where the basic structures and physical processes are controlled by the magnetic fields/electric currents of the particular region. The physical parameters of quiescent, or nonflaring, structures in the low solar corona and upper chromosphere have been inferred from nearly simultaneous spectral polarization observations (RATAN 600) and high-spatial-resolution radio observations (VLA). They have been compared with images from the Soft X-ray Telescope (SXT) aboard the *Yohkoh* satellite, indicating that bright radio (20 cm) and X-ray structures coincide, but that there is radio emission that is not detectable at X-ray wavelengths. Variable soft X-ray emission on time scales of hours suggests continued, varying, low-level heating or particle acceleration in localized areas of active regions. The RATAN-600 observations have been combined with the theory of thermal cyclotron emission to infer magnetic field strengths in the low corona above practically all large sunspots with an accuracy of 2 or 3%. They indicate that the magnetic field strength of the thermal plasma at the million-degree level above large sunspots is 75%–80% of the magnetic field strength in the underlying photospheric sunspots. The evolution of the magnetic structures is specified. Coronal potential field extrapolations are also provided, suggesting that the magnetic fields in the corona diverge more slowly than expected from a simple dipole located below the surface. Theoretical models are compared with multiple-wavelength VLA observations and potential field extrapolations, indicating that the radio emission from one active region can be explained by thermal gyroresonance radiation in a conductive flux model. However, the high brightness temperature and steep spectrum of the radio emission of another active region cannot be explained by conventional thermal models, and instead suggest long-lasting nonthermal heating in localized coronal sources above the magnetic neutral line in the underlying photosphere. Gyrosynchrotron radiation of nonthermal electrons cannot explain the observations of one such source, but heating within a localized neutral current sheet might account for them. Long-lasting radio sources with high brightness temperatures $\geq 10^7$ K and steep radiation spectra are often associated with active regions with a multipolar δ configuration of the photospheric sunspots. These "peculiar" coronal radio sources appear above the magnetic neutral line in the photosphere, and appear to require nearly continuous acceleration of energetic nonthermal electrons by a yet unknown process.

Subject headings: polarization — Sun: activity — Sun: corona — Sun: magnetic fields — Sun: radio radiation — Sun: X-rays, gamma rays

1. INTRODUCTION

The strong magnetic fields of solar active regions shape and constrain the structure of the solar atmosphere above the photosphere. These include the regions of higher density and/or temperature in the solar corona (such as coronal loops) and local areas of release of nonthermal energy. It seems natural to call these regions of the corona and the chromosphere the *magnetosphere* of the active region.

Until recently these *magnetospheres* were hardly accessible to direct observations; but large radio telescopes are, when used simultaneously, now capable of presenting both high spatial resolution and detailed spectral-polarization analysis in a wide wavelength range (e.g., Bogod et al. 1992). Such observations present unique information on the structure and strength of the magnetic fields in the thermal corona above active regions and can additionally measure temperatures and electron densities in different plasma structures. The spectral microwave observations also delineate long-lasting local regions of nonthermal energy release—the so-called *peculiar sources* (Akhmedov et al. 1986). The hot coronal loops are also now observed with X-ray telescopes in space, and here we additionally compare the radio images of specific active regions with soft X-ray images taken with the *Yohkoh* satellite.

In this paper we present observations made on 1992 January 9 and 10 and 1992 May 1 and 2 with the new Panoramic Spectrum Analyzer (PSA) on the RATAN-600 radio telescope in the wavelength range 1.7 to 32 cm and with the Very Large Array (VLA) at wavelengths of 2.0, 3.5, 6.2, and 20.7 cm. These radio data were combined with magnetograph data from Kitt Peak and soft X-ray images from the *Yohkoh* satellite, resulting in the study and comparison of the magnetospheres of a number of active regions.

2. RATAN-600 OBSERVATIONS

The RATAN-600 was used to observe the Sun on 1992 January 9 and 10 and on 1992 May 1 and 2 with the new PAS at 27 wavelengths between 1.7 and 32 cm (for a description of the PSA see Bogod et al. 1993). The observations were made in the "antenna mode" in which a flat, tiltable mirror is used to direct the solar radiation toward the southern sector of the primary ring (cf. Khaikin et al. 1972; Parijskij et al. 1976). A secondary reflector then collects and focuses the signal on a set of six microwave receivers which comprise the PSA. In this mode of operation, observations of both total intensity and circular polarization at different azimuths can be combined to specify the position of sources on the Sun. The half-power beamwidths at each wavelength are given in Table 1.

In 1992 January the observations of the Sun with the RATAN-600 were made daily near 9:20 UT (the local noon). Figure 1 presents radio scans of the solar disk on 1992 January 9 in total intensity, I, and circular polarization, or Stokes parameter, V, together with an optical map of the Sun as published in the bulletin Solnechne Danneye. Figure 2 shows similar radio and optical observations on January 10.

The radio scans of total intensity show the presence of enhanced radio emission above sunspots at all wavelengths, with a strong dependence of their intensity on the wavelength of observation. The most intense sources are associated with a group of five active regions, AR 6996, AR 6998, AR 7003, AR 7005, and AR 7006 in the north near central meridian, and with two active regions, AR 6993 and AR 6994, in the southwest. The RATAN data show that both the total intensity and circular polarization of the different sources was relatively constant over the 2 days of observation. The polarization scans reflect the strength and structure of the magnetic fields. Nearly every large sunspot has its own polarized source of radio emission. The sign of polarization is usually determined by the polarity of the magnetic field at the photospheric level (right-handed polarization for north polarity of the photospheric magnetic filed and left-handed polarity for south polarity in the photosphere); it corresponds to the extraordinary mode of wave propagation.

TABLE 1

WAVELENGTHS AND ANGULAR RESOLUTION AVAILABLE WITH THE PSA[a]

	ANGULAR RESOLUTION	
λ cm	E-W (″)	N-S (′)
30.0	270.0	187
20.0	180.0	125
12.0	108.0	75
8.21	75.0	52
7.79	70.0	48
7.24	65.0	45
6.86	61.0	42
6.49	58.0	40
6.10	55.0	38
5.83	52.5	36
5.58	50.0	34
5.28	47.5	33
5.00	45.0	31
4.73	42.6	30
4.60	42.0	29
4.36	40.0	27
4.15	37.0	26
4.02	36.0	25
3.86	34.0	24
3.65	33.0	23
3.45	31.0	21
3.22	29.0	20
3.10	28.0	19
2.94	26.5	18
2.80	25.0	17
2.68	24.0	17
2.56	23.0	16
2.40	21.6	15
2.30	20.7	14
2.20	20.0	14
2.10	19.0	12
2.00	18.0	12
1.90	17.1	12
1.80	16.2	11
1.71	15.4	10

[a] The angular resolution is the full width to half-maximum of the antenna beam pattern.

Daily scans were also made at local noon in May 1992. The results for 1992 May 1 and 2 are shown in Figures 3 and 4 where the scans of the full disk are shown together with the maps of the magnetic fields from the bulletin Solnechne Danneye. The radio sources of the two active regions (AR 7143 and AR 7150) seen on both days in May have quite different peak brightness temperatures (Fig. 5). At all centimeter wavelengths the brightest source is associated with AR 7143. A narrow, intense, source which is usually identified with the cyclotron emission of thermal coronal electrons at the third harmonic of the gyrofrequency, is observed in AR 7143 for $\lambda \geq 2.3$ cm on May 2. The radio emission of AR 7143 is polarized at $\lambda \geq 2.8$ cm (magnetic field strength of $B = 1550$ G at the third harmonic); with a degree of polarization of $\rho_c \approx 11\%$ at $\lambda = 4.0$ cm.

The angular size, θ_s, and flux, S_λ, of each sunspot-associated source was obtained from the RATAN radio profiles using a Gaussian-fitting routine. The average brightness temperature at each wavelength was then calculated from the source size and flux under the assumption of circular symmetry. As shown in Figure 5, the compact source associated with AR 7143 has a peak brightness temperature of $T_b = 1.5 \times 10^6$ K, with a sharp decrease in brightness temperature at wavelengths longer than about 3.5 cm. In contrast, the peak brightness temperatures of the two components b and c in AR 7150 (see Fig. 3) have peak brightness temperatures of $T_b = 3\text{–}5 \times 10^5$ K. We point out that these values are lower limits to the true brightness temperatures for both active regions because the measured angular sizes of $\theta_s \approx 30''$ are comparable to the sizes of the RATAN beams. For example, when a correction is made for the smaller angular sizes obtained from the VLA maps for AR 7143 ($\theta_s \approx 12''$ at 3.5 cm and $\theta \approx 22''$ at 6.1 cm), we infer a peak brightness

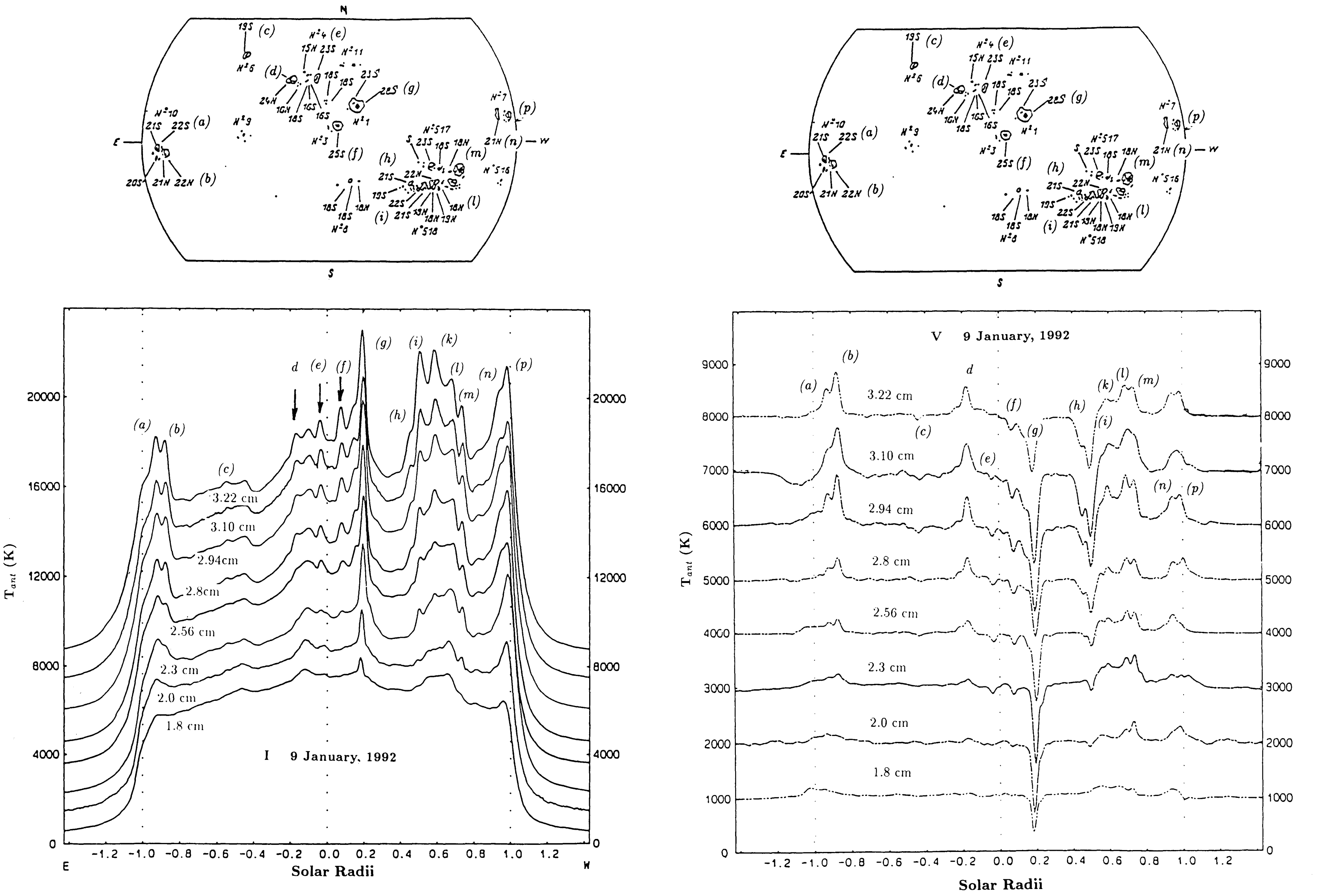

FIG. 1.—One-dimensional fan beam scans of total intensity, *I*, and Stokes parameter, *V*, made with the RATAN-600 PSA on 1992 January 9. The optical map of sunspots and their magnetic fields, obtained from the bulletin Solnechnye Dannye, are also presented. The peak magnetic field strengths of the sunspots are expressed in units of hundreds of gauss, where N and S denote positive and negative polarity, respectively.

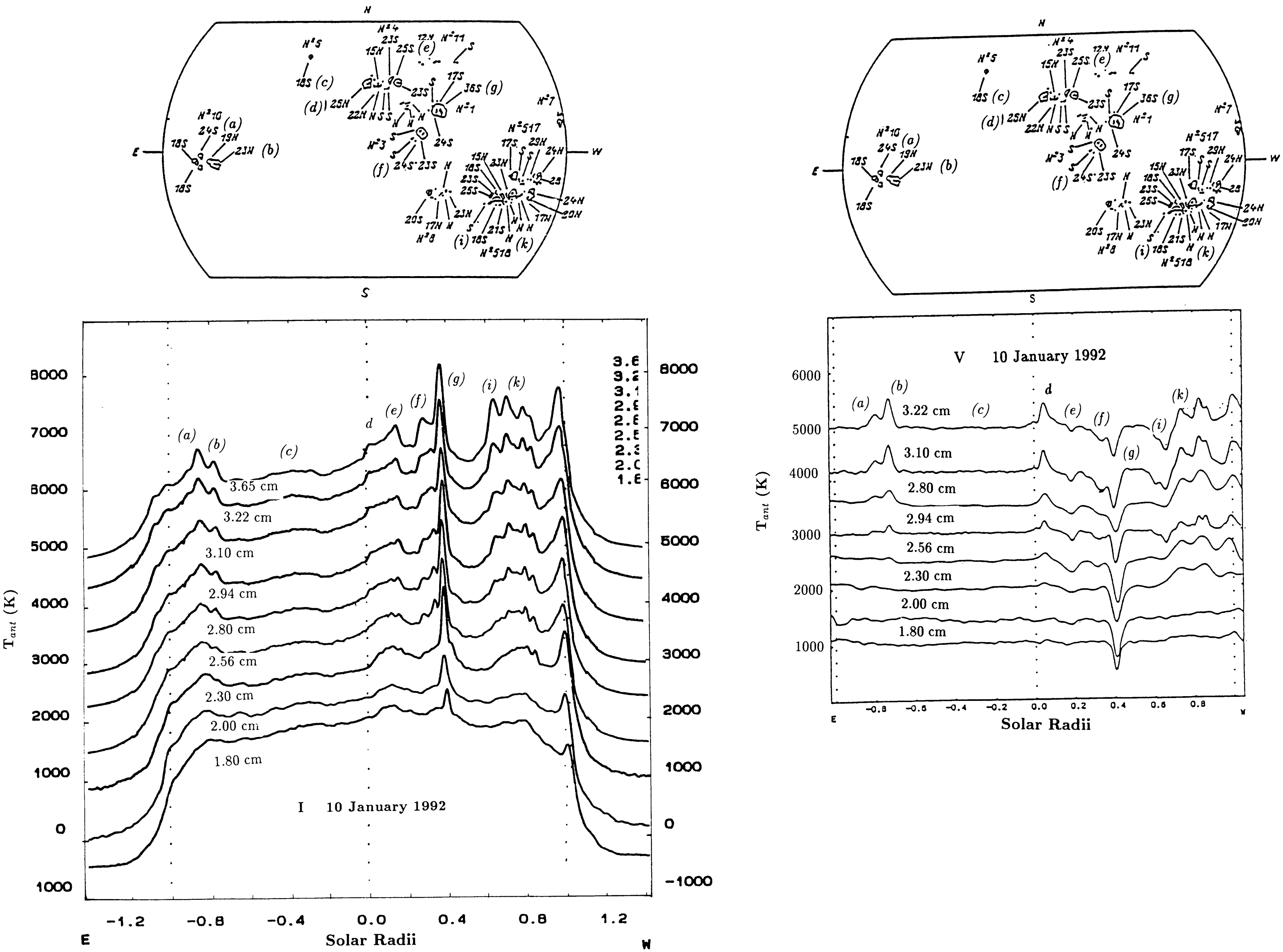

FIG. 2.—One-dimensional fan beam scans of total intensity, I, and Stokes parameter, V, made with the RATAN-600 PSA on 1992 January 10. The optical map of sunspots and their magnetic fields are also presented.

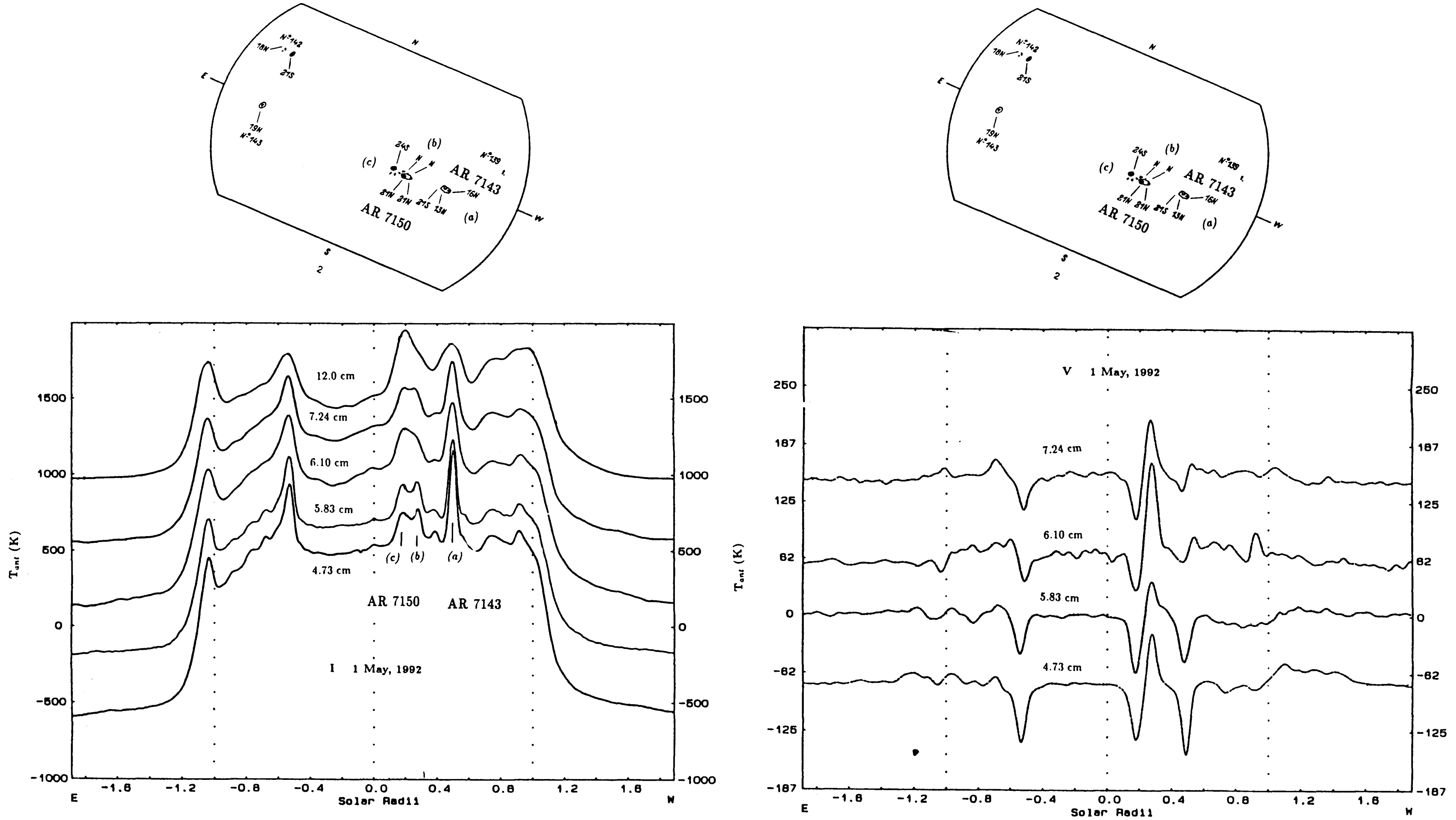

FIG. 3.—One-dimensional fan beam scans of total intensity, *I*, and Stokes parameter, *V*, made with the RATAN-600 PSA on 1992 May 1. The optical map of sunspots and their magnetic fields are also presented.

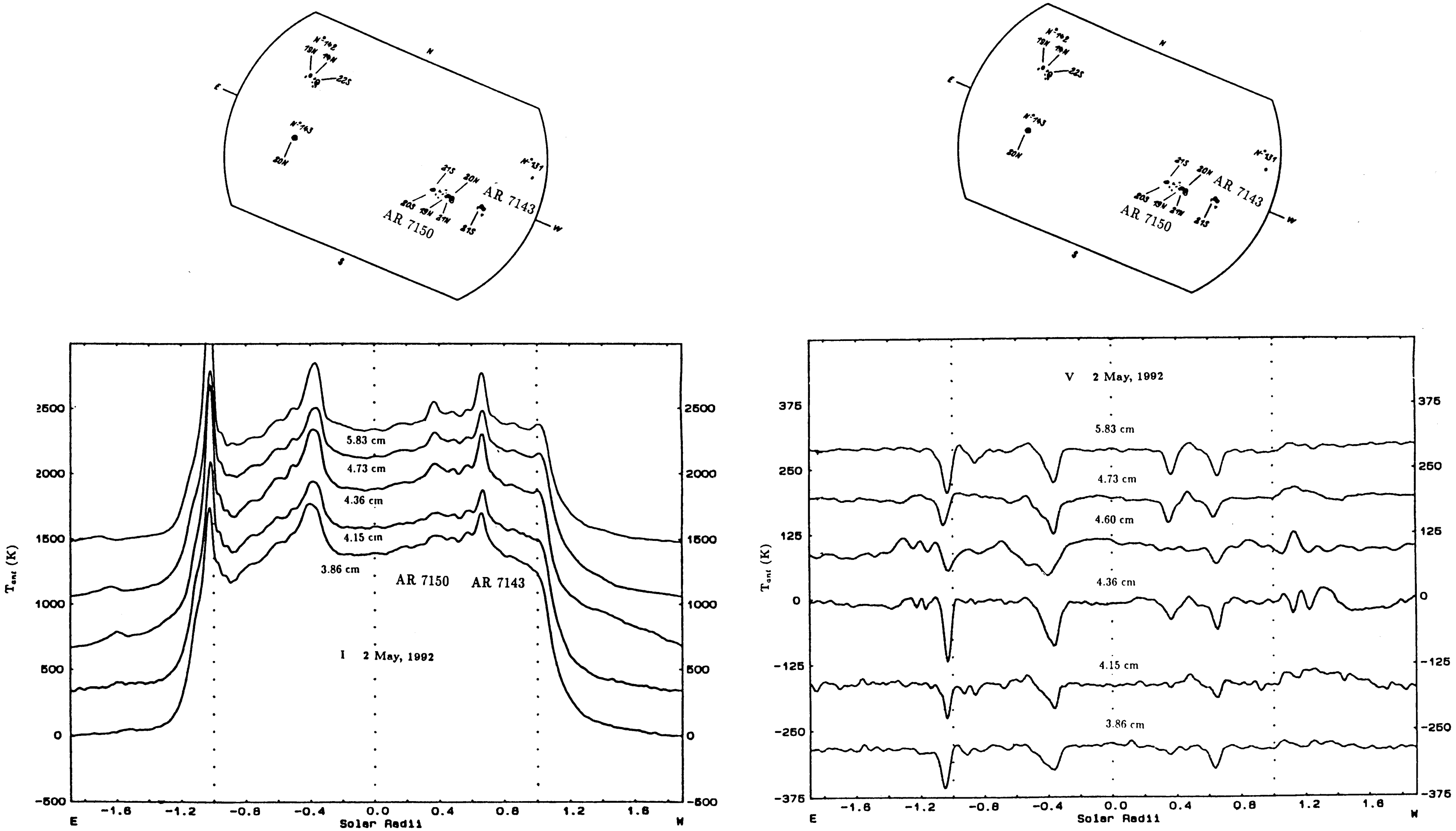

FIG. 4.—One-dimensional fan beam scans of total intensity, *I*, and Stokes parameter, *V*, made with the RATAN-600 PSA on 1992 May 2. The optical map of sunspots and their magnetic fields are also presented.

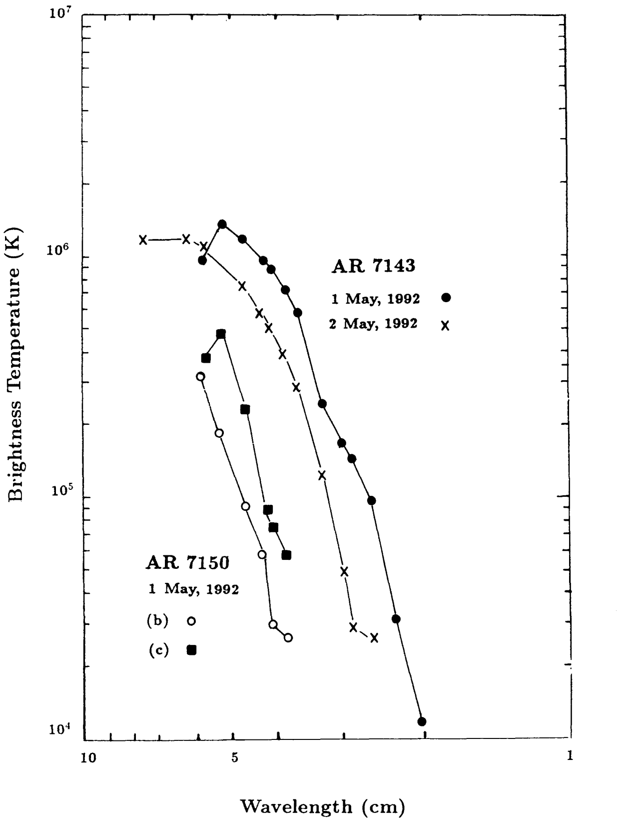

FIG. 5.—RATAN-600 brightness temperature spectra for the core sources associated with AR 7150 on 1992 May 1 and for the active region AR 7143 on 1992 May 1 and 2.

temperature of $T_b \approx 4 \times 10^6$ K at 3.5–6.0 cm, in reasonably good agreement with those obtained from the VLA maps.

The shortest wavelength at which sunspot-associated sources appear in AR 7150 is $\lambda = 3.5$ cm, both for the leading and following sunspots in the bipolar sunspot group. This corresponds to a coronal magnetic field strength of $B = 980$ G at the third harmonic. The radio emission associated with AR 7150 shows a bipolar polarization structure for $\lambda \geq 4.1$ cm with the usual dominance of the extraordinary mode above the main sunspots of the group. The degree of polarization of the sunspot-associated sources is $\rho_c \approx 15\%$ at $\lambda = 4$–6 cm.

There was a change in the structure of the radio source of AR 7150 which took place between May 1 and 2. On May 1, the brighter source was the one connected with the leading spot, while on May 2 the brighter region at all wavelengths was located above the following spot. This change is not due to a flare or burst because both regions of dominant emission lasted for days.

3. VLA OBSERVATIONS

The VLA was used to observe the full solar disk at 20.7 cm (1446 MHz) between 15:00 and 20:00 UT on January 9 and between 20:00 and 24:00 UT on January 10. During this time the array was in the B-configuration which provided a synthesized beamwidth of $\approx 5''$. The data were obtained using a time resolution of 1.67 s and a bandwidth of 12.5 MHz. The full solar disk was observed at 20.7 cm for 40 minute periods followed by 5 minute observations of the calibration source PKS 1819−096.

On 1992 January 9 and 10 the most intense radio emission was associated with the complex of five active regions in the northern hemisphere, and in Figure 6 we show VLA synthesis maps at 20.7 cm wavelength for these regions. The radio image for January 9 has been overlaid on contours of photospheric magnetic fields as measured on a Kitt Peak magnetogram (taken at 15:33:32 UT) while the image for January 10 is compared with an optical map of the sunspots made at the Kislovodsk Observatory. The map for January 9 shows a complicated configuration of looplike structures that extend across areas of opposite magnetic polarity and also interconnect the five active regions. These sources have peak brightness temperatures of $T_b = 1$–2×10^6 K and show no circular polarization above $\rho_c \approx 15\%$. On January 10, looplike sources with $T_b \approx 2 \times 10^6$ K are also detected, although significant changes in the structure can also be seen. For example, the diffuse emission connecting AR 7003 and AR 7006 on January 9 has disappeared as has the source associated with AR 6998. These differences in source structure may reflect changes in the coronal magnetic fields above the sunspots.

On 1992 May 1 the VLA was used to observe active regions AR 7143 (S05 W33 at 1300 UT) and AR 7150 (S07 W16) between 14:00 and 23:30 UT. These observations were carried out as part of the Coronal Magnetic Structures Observing Campaign (COMStOc 92). AR 7143 was observed alternately at $\lambda = 3.5$, 6.2, and 20.7 cm, and AR 7150 at $\lambda = 2.0$, 3.5, 6.2, and 20.7 cm for 20 minute periods followed by 5 minute observations of the phase calibration source 3C 48 every 40 minutes. At the time of these observations, the VLA was in the C-configuration which provided synthesized beamwidths of $1''.2$, $2''.1$, $4''.0$, and $12''.6$ at $\lambda = 2$, 3.5, 6.2, and 20.7 cm, respectively.

The data were edited and calibrated using the standard VLA data reduction packages and used to produce synthesis maps of total intensity, I, and Stokes parameter, V, at each wavelength.

In Figure 7 we compare a VLA 20.7 cm map of total intensity on May 1 with a Kitt Peak magnetogram and a soft X-ray image taken by the Soft X-ray Telescope (SXT) on board the *Yohkoh* satellite. This figure shows bright radio and X-ray emission above both AR 7143 and AR 7150 as well as the smaller active region AR 7146 to the north. In Figures 8 and 9 we show synthesis maps of AR 7143 and AR 7150 at 2.0, 3.5, 6.2, and 20.7 cm together with *Yohkoh* soft X-ray images and maps of the underlying photospheric fields.

The VLA 20.7 cm maps show bright ($T_b \approx 2 \times 10^6$ K—Table 2) unpolarized ($\rho_c \leq 5\%$) sources whose peaks lie along the magnetic neutral line. The soft X-ray and 20 cm peaks for both active regions coincide, and for AR 7150, there is also bright 20 cm emission above sunspots and regions of low X-ray emission. This result is consistent with previous comparisons of soft X-ray and 20 cm loops which show bright radio sources that coincide with the soft X-ray sources as well as bright radio sources with no detectable X-ray emission (e.g., Lang et al. 1987a, b; Brosius et al. 1992). The shorter wavelength emission from AR 7150 ($\lambda = 2.0$, 3.5, and 6.2 cm) consists of several components having moderate degrees of circular polarization ($\rho_c = 20\%$–58%) and brightness temperatures of $T_b = 0.2$–1.2×10^6 K. The peak brightness temperature, $T_{b_{\max}}$, and maximum degree of circular polarization, ρ_c, for each VLA component is given in Table 2. The sources at 3.5 and 6.2 cm lie close to the main sunspots whereas the most intense 2 cm source ($T_b \approx 2 \times 10^5$ K) lies between two regions of opposite magnetic polarity.

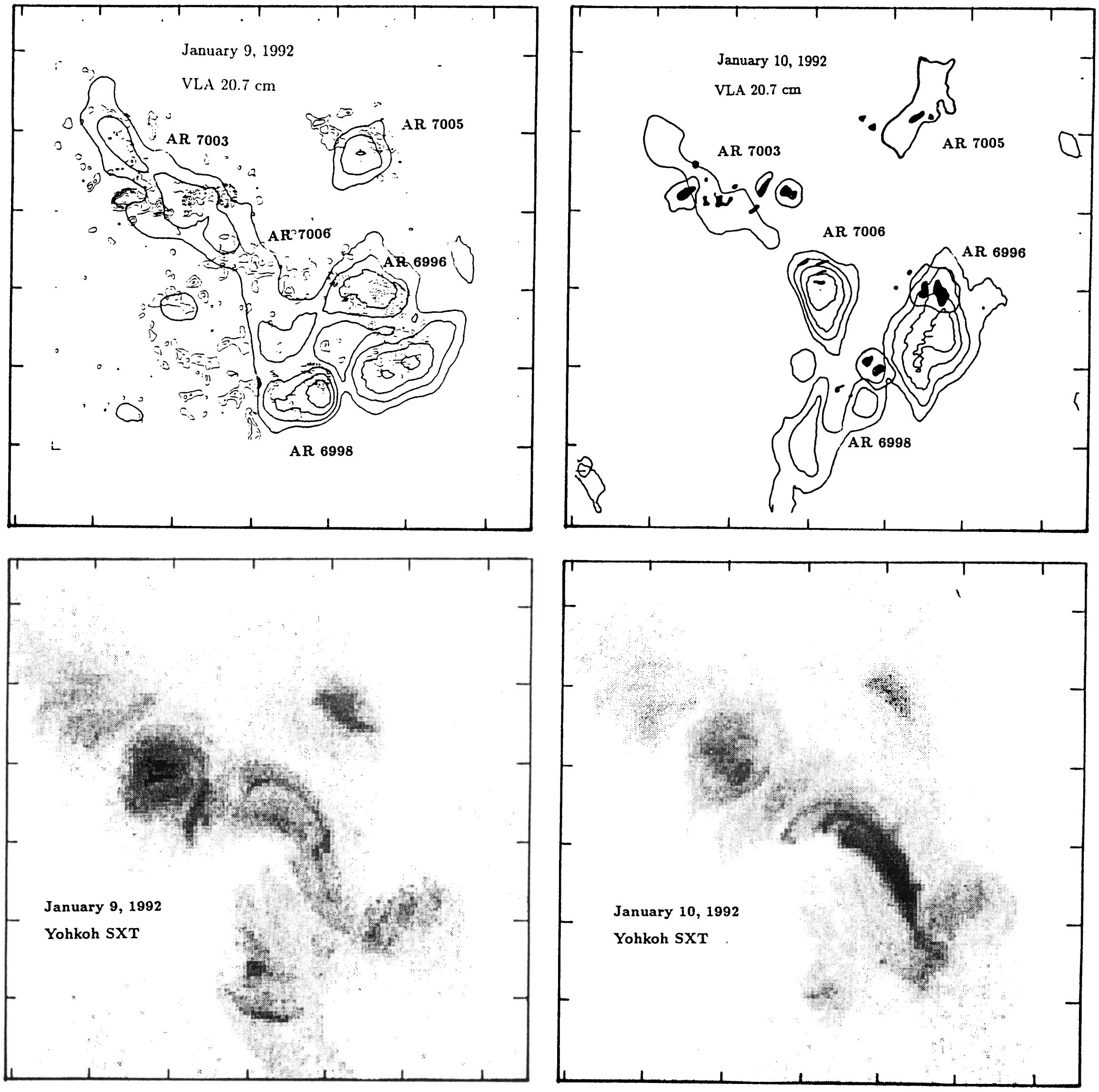

FIG. 6.—VLA synthesis maps of total intensity at 20.7 cm on January 9 (*left*) and 10 (*right*) are compared with contours of photospheric magnetic fields as measured on a Kitt Peak magnetogram (Januaty 9) and with an optical map showing the underlying sunspots (January 10). The bottom panels show gray-scale soft X-ray images obtained from the Soft X-ray Telescope (SXT) on board the *Yohkoh* satellite. The radio contours mark levels of equal brightness temperature, T_b, with an outermost contour and contour interval equal to 4.2×10^5 K. The outermost contour and contour interval of the magnetic fields are equal to 300 G, with solid and dashed contours corresponding to positive and negative fields, respectively. The angular scale may be determined from the 100″ spacing between the fiducial marks on the axes.

TABLE 2

PARAMETERS OF THE VLA SOURCES

Active Region	λ (cm)		$T_{b_{\max}}$ (K)	ρ_c (%)
AR 7143…………	3.5		4.6×10^6	≤ 5
	6.2		2.4×10^6	≤ 5
	20.7		1.4×10^6	≤ 10
AR 7150…………	2.0		2.0×10^5	≤ 5
	3.5	X1	9.7×10^5	58
	3.5	X2	3.6×10^5	≤ 10
	3.5	X3	3.0×10^5	≤ 10
	6.2	C1	1.1×10^6	40
	6.2	C2	8.8×10^5	5
	6.2	C3	8.5×10^5	≤ 10
	6.2	C4	6.6×10^5	0
	20.7		1.9×10^6	≤ 10

In contrast, the 3.5 and 6.2 cm emission from AR 7143 is confined to a single compact source with a brightness temperature of $T_b = 4.6 \times 10^6$ K at 3.5 cm and $T_b = 2.4 \times 10^6$ K at 6.2 cm. These sources lie along the magnetic neutral line, suggesting that they occur near the top of a coronal loop that joins regions of opposite magnetic polarity. The relatively high brightness temperatures at these shorter wavelengths are consistent with those derived from the RATAN data and suggest some sort of nonthermal heating of the coronal plasma in this active region (see § 8).

4. *YOHKOH* SOFT X-RAY OBSERVATIONS

On January 9 and 10 and on May 1, the SXT on board the *Yohkoh* spacecraft observed the Sun throughout the periods of VLA observations. The SXT is a broad-band soft X-ray

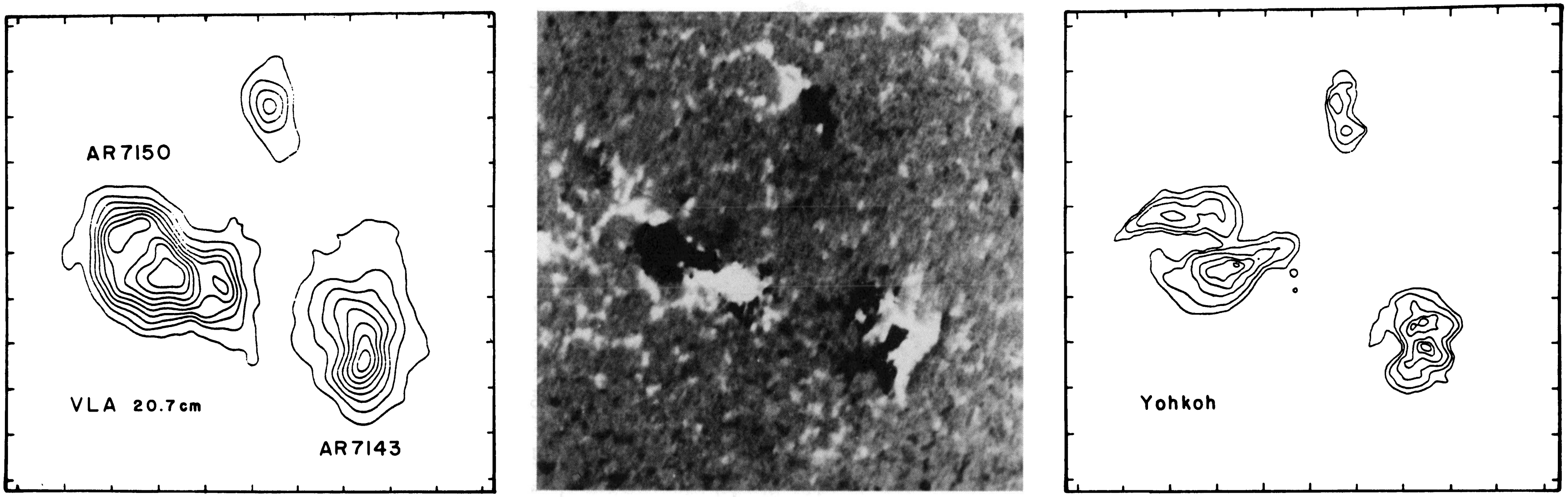

FIG. 7.—A VLA 20.7 synthesis map of total intensity (*left*) on 1992 May 1, is compared with a Kitt Peak magnetogram (*middle*) and a soft X-ray image (*right*) taken at 16:43:41 UT by the *Yohkoh* satellite. Each image has the same 10′.5 field of view, with a fiducial mark spacing of 60″. The contours of the VLA map mark levels of equal brightness temperature, T_b, with an outermost contour and contour interval equal to 1.9×10^5 K. The *Yohkoh* soft X-ray image represents a section of a 42′ raster with 5″ steps that took 2.7 s to complete. Contour levels are 500, 1000, 2000, 4000 . . . counts.

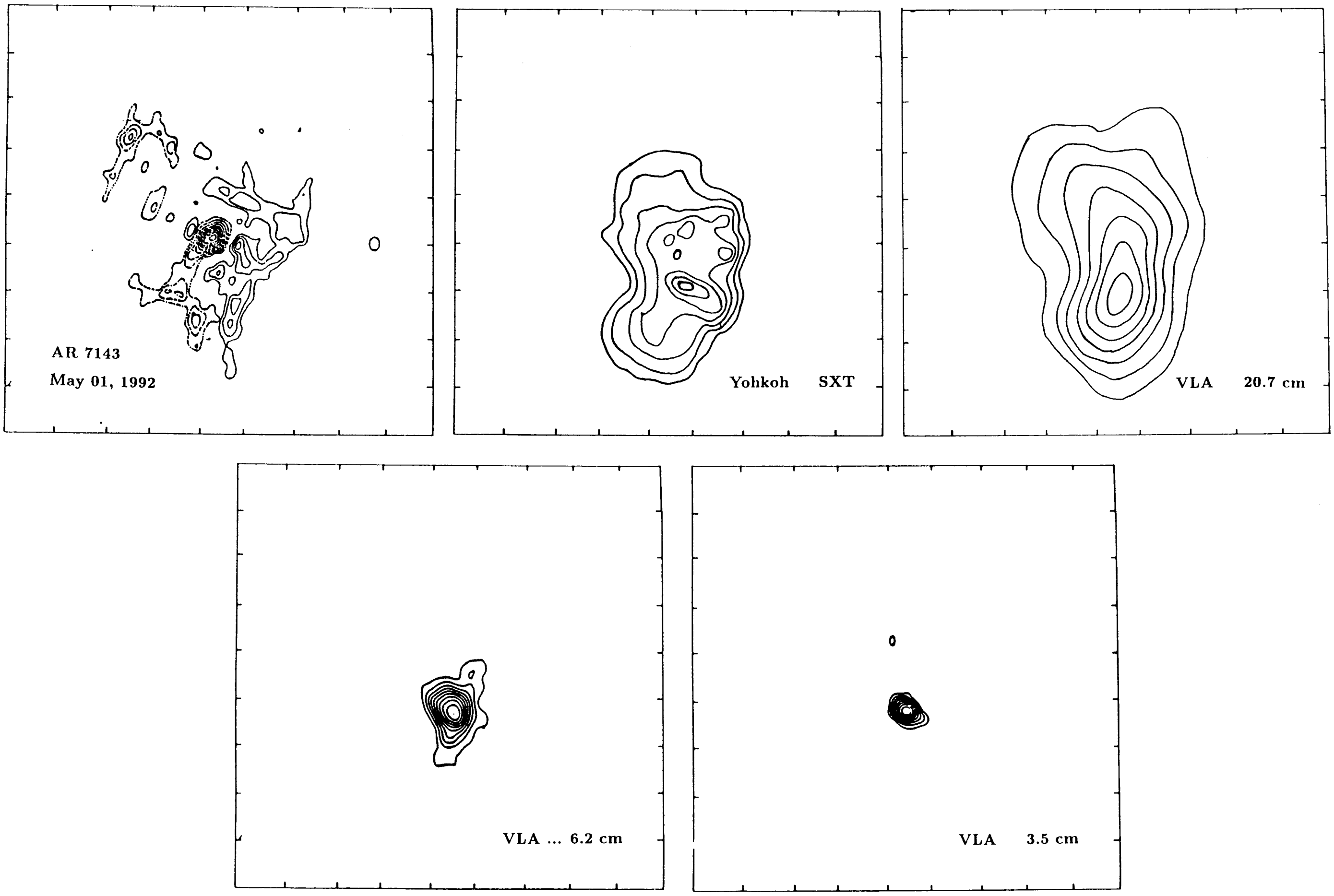

FIG. 8.—Observations of the active region AR 7143 on 1992 May 1. All of the boxes have the same 4'.5 field of view, with a fiducial mark spacing of 30". The VLA synthesis maps of total intensity at 3.5, 6.2, and 20.7 cm have the following outermost contours and contour intervals: 3.5 cm–9.2 × 10^5 K, 4.6 × 10^5 K; 6.2 cm–4.8 × 10^5 K, 2.4 × 10^5 K; 20.7 cm–4.2 × 10^5 K, 1.4 × 10^5 K. The contours of the Kitt Peak magnetogram, taken at 14:43:40 UT, mark levels of equal longitudinal magnetic field strength with an outermost contour and contour interval equal to 300 G. The *Yohkoh* soft X-ray map, made at 16:43:41 UT, is a section of a full-disk image that was accumulated during a 42' raster with 4".92 steps which took 2.7 s, to complete. Contour levels are 500, 1000, 2000, 4000 ... counts.

grazing incidence telescope which records its images with a 1024 × 1024 CCD (Tsuneta et al. 1991). The instrument has five thin-metal filters which can be selected to provide broadband temperature diagnostics. On 1992 May 1, full disk images (42' × 42') were obtained about three or four times during each orbit. On May 1 the SXT also centered its partial frame 4' prime field of view on AR 7150. The partial frame images were obtained with 2".45 pixels using the thin and thick Al filters, whereas the full-disk images were obtained at half-resolution with 5".9 pixels using the thin Al and composite (Al/Mg/Mn) filters. The full disk images on May 1 included the nearby active region AR 7143 whose radio emission was detected by the VLA and the RATAN. The SXT Aspect Telescope also provided white-light sunspot images that were used to co-align the VLA and soft X-ray images.

The electron temperature and emission measure were estimated from the partial-frame images on May 1 for AR 7150 at 15:01 UT and 18:33 UT. The brightest regions were summed and the ratio of the emissions from the two filters was used to obtain temperatures and emission measures, assuming an isothermal plasma. At 15:01 UT the two brightest regions had temperatures of $T_e = 6 \pm 0.8 \times 10^6$ K and emission measures of 2.3 × 10^{44} cm^{-3} (leading portion) and 2.9 × 10^{44} cm^{-3} (trailing portion). At 18:33 UT the trailing portion decreased in signal strength and produced a temperature of $T_e = 5 \pm 3 \times 10^6$ K and emission measure of 7 × 10^{43} cm^{-3}. The leading portion of the region had $T_e = 5 \times 10^6$ K and an emission measure of 1 × 10^{44} cm^{-3}. The quoted uncertainties of the electron temperatures are 1 σ statistical errors.

The measured temperatures are somewhat higher than expected for active regions, but correspond to results from other active regions observed with the SXT (e.g., Hara et al. 1992). This is probably caused by the fact that the SXT response function is rising steeply at 1–10 × 10^6 K, and thus, an isothermal analysis will be weighted toward the plasma with the highest electron temperatures. On some occasions three or more filters have been included in the observing sequence (Hara et al. 1992). From such data sets it is possible to determine that a lower temperature component is also present. In the AR 7150 images analyzed here, the lowest temperature detected from portions of the images with sufficient statistical signal was about 4 × 10^6 K.

In the bottom panels of Figure 6 we show SXT maps of the northern complex of active regions observed on January 9 and 10. These images show bright X-ray sources above each of the five regions as well as fainter emission which appears to inter-

1993ApJ...419..398L

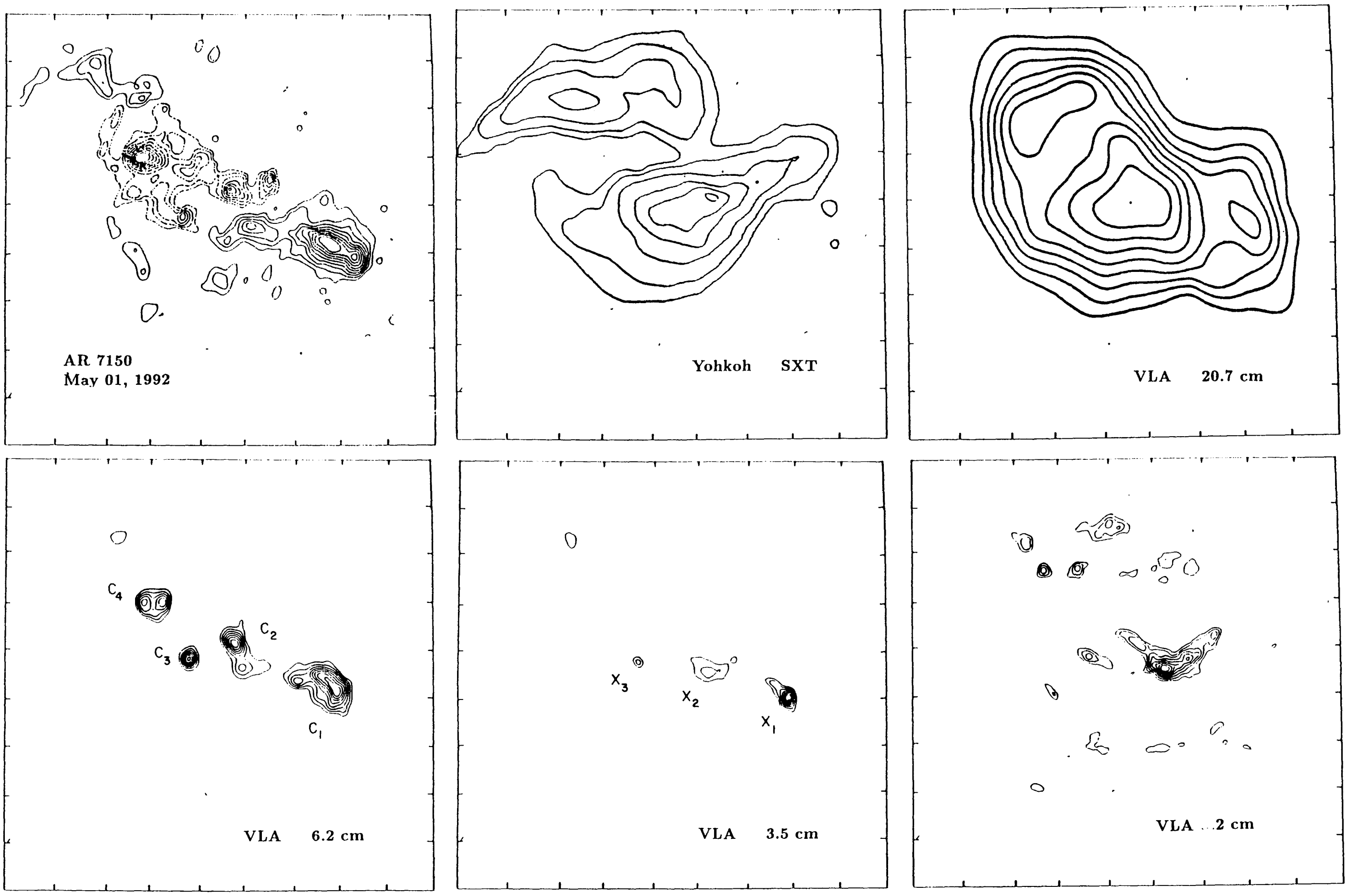

FIG. 9.—Observations of the active region AR 7150 on 1992 May 1. All of the boxes have the same 4'.5 field of view with a fiducial mark spacing of 30". The VLA synthesis maps of total intensity at 2.0, 3.5, 6.2, and 20.7 cm have the following outermost contours and contour intervals: 2.0 cm–4.1×10^4 K, 2.0×10^4 K; 3.5 cm–2.4×10^5 K, 1.2×10^5 K; 6.2 cm–2.2×10^5 K, 1.1×10^5 K; 20.7 cm–3.8×10^5 K, 1.9×10^5 K. The contours of the Kitt Peak magnetogram and *Yohkoh* soft X-ray image are the same as those given in Fig. 7.

connect them. Subtle changes in X-ray brightness are detected in some regions (especially AR 6998) and similar variations can also be seen in the VLA 20 cm maps. A detailed analysis of these SXT images and their relationship to large-scale coronal loops and long-lasting noise storm activity will be discussed elsewhere (Lang et al. 1993).

In Figure 10 we present a series of SXT images which show the structure of the X-ray emission from AR 7143 and AR 7150 at different times. During the beginning of the VLA observations (14:57:03 UT and 15:18:23 UT) the brightest X-ray source in AR 7150 was a looplike structure (L_1) located in the northeast part of the active region. This loop faded, then reappeared later in the day (19:47:15 UT). An examination of the *GOES* soft X-ray plots and Solar Geophysical Data shows that neither of these brightenings were associated with detectable soft X-ray bursts or Hα flares. These changes instead appear to represent some sort of continued, varying low-level heating or particle acceleration in localized areas of the active region and which are undetected by full-Sun detectors such as *GOES*.

The X-ray emission from AR 7143 showed only small changes through the day, notably some subtle brightenings at the northern end of the region.

5. MAGNETIC FIELDS ABOVE SUNSPOTS AS DETERMINED FROM THE RADIO DATA

One radio method of measuring magnetic fields above sunspots is based on the analysis of the radio spectra of emission generated by thermal cyclotron (or gyroresonance) radiation. For most cases of practical interest, simple model estimates show that one should take into account the second or third harmonic of the electron gyrofrequency ($\nu_B = eB/m_e c$, $\approx 2.8 \times 10^6 B$, where e is the charge on the electron, B is the magnetic field strength, m_e is the mass of the electron, and c is the speed of light) (Shevagaonkar & Kundu 1984, 1989). This implies that observations at a particular wavelength λ refer to the regions with magnetic field strengths B in Gauss given by

$$B = \frac{5350}{\lambda} \, (s = 2) \, ,$$

$$B = \frac{3570}{\lambda} \, (s = 3) \, , \tag{1}$$

where s is the harmonic number and λ is the wavelength in centimeters. We may often distinguish between the second and

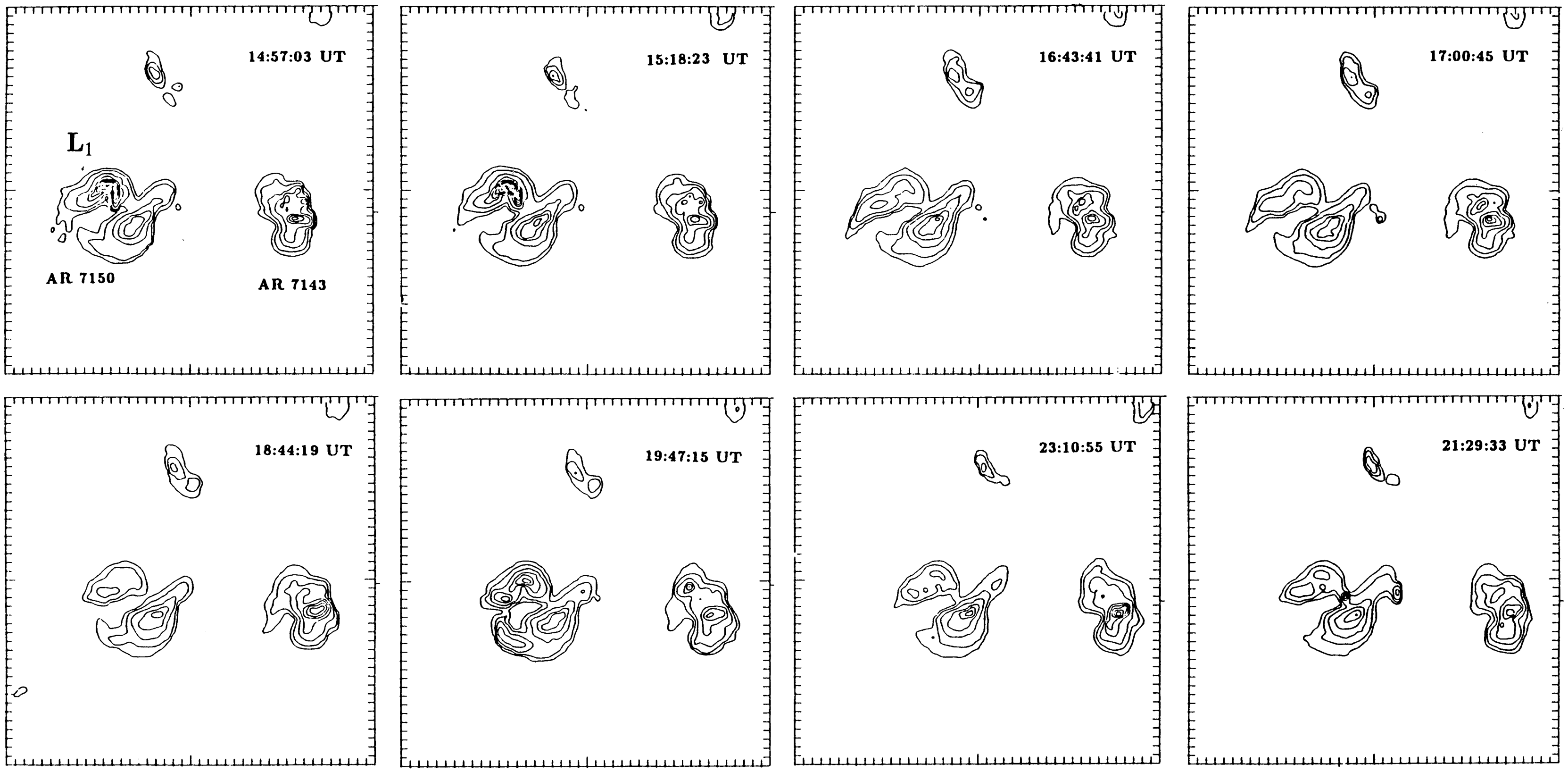

FIG. 10.—A series of *Yohkoh* soft X-ray images of AR 7143 and AR 7150 on 1992 May 1 taken at the times indicated. Each image is a 10′.5 section of a full-disk image that was accumulated during a 42′ raster with 4″.92 steps which took 2.7 s to complete. Each image has the same 10′.5 field of view with a fiducial mark spacing of 15″. Contour levels are 500, 1000, 2000, 4000 . . . counts.

third harmonics using polarization measurements (in the case of positive temperature gradients the third harmonic is strongly circularly polarized). Since the extraordinary mode of radiation is more intense than the ordinary one, we can also infer the polarity of the magnetic field. The shortest wavelength, λ_{crit}, generated at the third harmonic by this mechanism determines the strongest magnetic field in the coronal region of the investigated structure.

The accuracy of this method depends both on the validity of models of the assumed radiation mechanism and on the accuracy of determining the wavelength λ_{crit}. Theoretical computations for any reasonable model of the solar atmosphere show that the third harmonic emission in the extraordinary mode is the most intense, while the emission of the ordinary mode can be an order of magnitude weaker and may be insignificant at the second harmonic. That implies a high degree of polarization of the third harmonic emission. There might be some detectable emission at the fourth harmonic which is also highly polarized. However, the difference between the optical thickness of the third and fourth harmonics is three to four orders of magnitude and the intensity ratio of the third to fourth harmonic decreases with temperature at the base of the corona. So, we can generally assume that the highly circularly polarized emission above sunspots is at the third harmonic, and such an assumption has been confirmed by a variety of observations (Brosius et al. 1992).

Thermal cyclotron radiation dominates the microwave radiation above large sunspots, with an observed polarization that is consistent with the expected extraordinary mode of wave propagation. The observed brightness temperatures, T_b, at the shorter centimeter wavelengths are between $T_b = 10^5$ K and $T_b \approx 2 \times 10^6$ K. Since the electron temperature $T_e \geq T_b$, our measurements refer to the low corona above sunspots where the electron temperature reaches a million degrees.

To be exact, $T_b = \tau T_e$, where the optical depth τ depends on both the electron temperature and the harmonic of the gyrofrequency. It can only reach the observed values of $\tau \geq 0.1$ for the third harmonic and an electron temperature of $T_e \approx 10^6$ K. Substantially higher temperatures are not observed in the corona and at substantially lower temperatures the optical depth decreases below the observed values for any harmonic. At a given temperature, the optical depth decreases by two orders of magnitude when going from the third to the fourth harmonic, and the second harmonic is inconsistent with the high degrees of circular polarization in the extraordinary mode. So, in quite general terms, we can say that our measurements refer to the third harmonic of the gyrofrequency in the million-degree corona above sunspots, and this has been confirmed by detailed models for specific active regions in § 7.

The unexpected result is that the measured radio value of the magnetic field strength $B_{\text{rad}} = 3570/\lambda_{\text{crit}}$, is only 20%–30% lower than that inferred from Zeeman-effect measurements in the underlying photosphere, B_{opt}, indicating that the magnetic field in the million-degree corona above sunspots is very strong—much stronger than may have been previously expected. This may be explained if the corona begins at a very low altitude above sunspots, or if there is a weak divergence of magnetic field lines that penetrate high in the solar atmosphere.

The new spectrum analyzer (PSA) at the RATAN-600 provides a spectral resolution of $\approx 5\%$ in the 1.7–4 cm wavelength range, with an $\approx 2.5\%$ accuracy in determining the critical wavelength λ_{crit} where the circular polarization above a particular sunspot disappears. Our determinations of the magnetic field strength B in the low corona above active regions have a comparable accuracy of at least 2.5%.

This method has been used to measure the magnetic fields above sunspots in the corona using observations made with the RATAN-600. Data on the strength of magnetic fields gained from these observations have been previously compared with optical measurements. (e.g., Akhmedov et al. 1982; Abramov-Maximov & Gelfreikh 1983; Bogod et al. 1982). An improvement in the accuracy of such measurements is now possible using the new spectrometer (PSA).

The multiwavelength RATAN polarization scans for January 9 and 10 (Figs. 1 and 2) reveal up to 14 sunspot-associated sources. Only one (marked g) is intense at the shortest wavelength of $\lambda = 1.8$ cm, implying that the coronal magnetic field in the corona exceeds 2000 G. Two sources (a and m), though weak, are still seen at this wavelength. Polarized emission begins at a longer wavelength for the other sources.

The results of the measurements of the coronal magnetic field strengths of these sunspot-associated sources are presented in Tables 3 and 4. In these tables LS denotes the local source as it is marked in Figure 2, SG denotes the number of the corresponding sunspot group in the monthly bulletin Solnechneye Danneye, B_{opt} and B_{rad} denote the magnetic field strengths found from optical and radio observations, λ_{crit} is the wavelength range for the shortest wavelengths of circularly polarized emission, and R and L denote right and left-hand circular polarization, respectively. The last column gives the parameter $\eta = B_{\text{rad}}/B_{\text{opt}}$, with a mean value of $\eta = 0.78$. These results therefore indicate that the magnetic fields above large sunspots are about 80% of the field strengths in the photosphere. They also confirm recent VLA observations of gyroresonance radiation at 2 cm which show that fields of up to 1800 G can exist in the corona above sunspot penumbrae (White, Kundu, & Gopalswamy 1991).

6. EVOLUTION OF PHOTOSPHERIC MAGNETIC STRUCTURES AND MODELS OF ACTIVE REGION MAGNETIC FIELDS

In this section we discuss the magnetic structure of the active regions as inferred from observations of the sunspots and coronal potential field extrapolations.

AR 7143 was observed daily from its appearance on the east limb on April 23. It had a δ-type configuration whose leading spot was of north magnetic polarity. During its passage across the disk, the total area of the spots decayed steadily from 475×10^{-6} to 25×10^{-6} of the visible solar hemisphere (Fig. 11).

AR 7150 appeared on the disk on April 28 and developed a normal bipolar magnetic structure with many small spots interspersed among the main ones. This group also produced numerous small flares (Solar Geophysical Data) during the few days before and after our common VLA-RATAN observations.

Thus, we were able to compare the magnetospheres of two active regions with different magnetic field structures, one a bipolar sunspot group (AR 7150), extending about 12° in longitude, the other (AR 7143) a magnetically complex group having a multipolar δ configuration with interspersed polarities.

In order to examine and compare the magnetic field structure above the two active regions, we used the potential field code developed by Sakurai (1982) to extrapolate the Kitt Peak

1993ApJ...419..398L

TABLE 3

The Magnetic Fields of the Sunspots on 1992 January 9

LS	Number SG	$B_{\rm opt}$	$B_{\rm rad}$	$\lambda_{\rm crit}$	η	Comments
a	10	21 S	18.9	2.00–1.80 *R*	0.90	Inver. of polar.
b	10	21 N	1.6	2.30–2.00 *R*	0.79	
c	6	19 S	14.7	2.56–2.30 *L*	0.77	
d	4	24 N	18.9	2.00–1.80 *R*	0.79	
e	4	23 S	16.6	2.30–2.00 *L*	0.72	
f	3	25 S	16.6	2.30–2.00 *L*	0.66	
g	1	28 S	>20.	$\leqslant$1.80 *L*	0.71	
h	518	21 S	14.7	2.56–2.30 *R*	0.70	
i	518	22 S	18.9	2.00–1.80 *L*	0.86	
k	517	23 S/18 N	16.6	2.30–2.00 *R*	?	Opt. identif.?
l	518	?		2.00–1.80 *R*	?	
m	517	?	20 (?)	1.80 (?)	?	
n	7	21 N	16.6	2.30–2.00 *R*	0.79	
o	7	...	16.6	2.30–2.00 *R*	?	Near the limb

TABLE 4

The Magnetic Fields of the Sunspots on 1992 January 10

LS	Number SG	$B_{\rm opt}$	$B_{\rm rad}$	$\lambda_{\rm crit}$	η	Comments
a	10	24 S	13.2	2.84–2.56 *R*	(0.55)	Inver. of polar.
b	10	21 N	16.6	2.30–2.00 *R*	0.79	
c	6	18 S	11.3	3.22–3.10 *L*	0.63	
d	4	26 N	16.6	2.30–2.00 *R*	0.64	
e	4	25 S	18.9	2.00–1.80 *L*	0.76	
f	3	23 S	14.7	2.56–2.30 *L*	0.64	
g	1	36 S	>20	$\leqslant$1.80 *L*	>0.56	
h	518	21 N	16.6	2.30–2.00 *R*	0.79	
i	518	26 S	18.9	2.00–1.80 *L*	0.73	
k	517/518	17 S/23 N	16.6	2.30–2.00 *R*	?	Opt. identif. ?
l + m	517/518	24 N/24 N	16.6	2.30–2.00 *R*	0.69	Opt. identif. ?
m	517	24 N	...	?	?	Identif. ?
n	7	?	16.6	2.30–2.00 *R*	0.79	Limb

photospheric fields into the corona. This code solves Laplace's equation to calculate current-free magnetic field lines using longitudinal photospheric fields as boundary conditions. It can also be used to calculate the magnetic field components B_x, B_y, and B_z at a constant height above the solar surface. The Kitt Peak magnetograms shown in Figures 6 and 7 were used to calculate individual field lines as well as maps of the total field at heights ranging from $h = 2000$–40000 km. Because the Kitt Peak magnetograms are known to saturate above $\approx$1000 G, the strong umbral fields were corrected by assuming that the spots could be represented as solenoids whose radii equalled the spots' photospheric radii (Sakurai & Uchida 1977). This method restores the missing flux to the magnetogram while leaving the weaker, unsaturated fields unchanged.

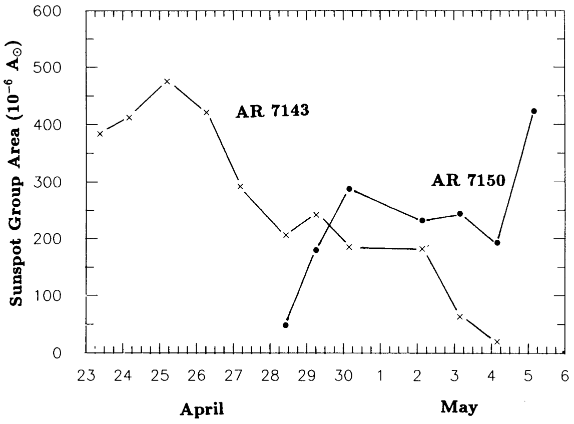

Fig. 11.—A plot of the total sunspot areas of the active regions AR 7143 and AR 7150 as a function of time.

In Figures 12 and 13 we show maps of the total field $B = (B_x^2 + B_y^2 + B_z^2)^{1/2}$ of AR 7143 and AR 7150, respectively, at heights of $h = 2000$, 10,000, and 20,000 km together with potential field lines at $h = 0$ km.

The extrapolation for AR 7143 (Fig. 12) reveals clusters of field lines joining the leading negative-polarity sunspot to the weaker and extended areas of positive polarity to the east and west. AR 7150 (Fig. 13) also shows two main sets of loops, labeled L_1 and L_2; the second set (L_2) appears to coincide with the bright soft X-ray loop observed during the first two hours of VLA observations (14:00–16:00 UT; see Fig. 10).

The potential field maps also provide measurements of the maximum field strength, $B_{\rm max}$, at different heights and therefore the vertical magnetic field gradient, $\Delta B/\Delta h$, in the corona. In Figure 14 we plot $B_{\rm max}$ as a function of height for the two active regions. Although both regions have comparable maximum photospheric fields of $B \approx 2100$ G, coronal potential fields decrease more rapidly with height above AR 7143. Between $h = 0$ km and 5000 km, the vertical gradient of the total field strength is $\Delta B/\Delta h = -0.30$ G km^{-1} for AR 7143 and $\Delta B/\Delta h = -0.21$ G km^{-1} for AR 7150. These values are comparable to the gradients obtained from magnetic field extrapolations for active regions recently studied by Brosius et al. (1992) and Bogod et al. (1992).

We may also use these results to determine whether the

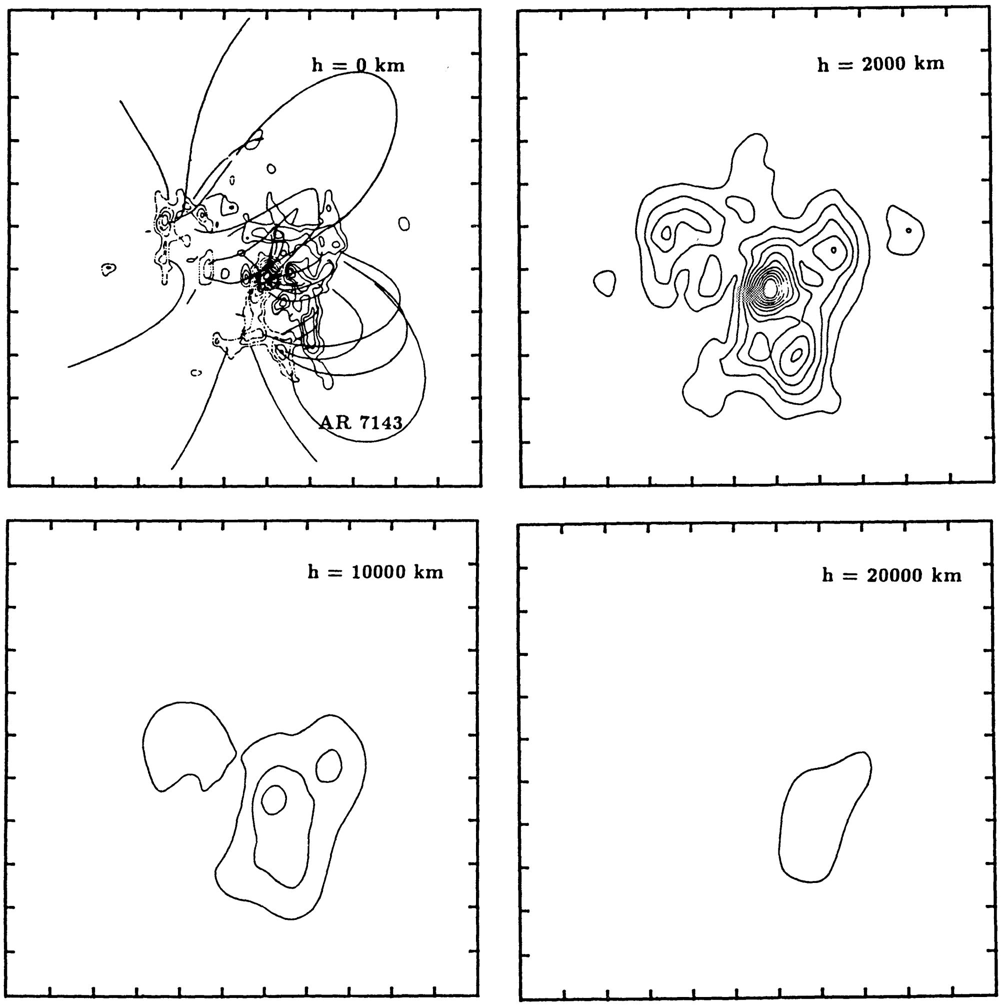

FIG. 12.—Contour map showing total extrapolated magnetic field strengths at heights of 0, 2000, 10,000 and 20,000 km for AR 7143 on 1992 May 1. Extrapolated field lines are also shown superposed on the Kitt Peak magnetogram ($h = 0$ km). The outermost contour and contour interval of the Kitt Peak magnetogram is equal to 200 G; those for the extrapolated field maps are equal to 100 G. The angular scale may be inferred from the 30″ fiducial marks on the axes.

vertical decrease in magnetic field strength is consistent with that expected from a magnetic dipole. For a vertically oriented dipole located a distance $y_{\rm phot}$ beneath the photosphere, the on-axis magnetic field strength $B(h)$ at a height h above the solar surface is (see Brosius & Holman 1988)

$$B(h) = B_{\rm phot}[(y_{\rm phot} + h)/y_{\rm phot}]^{-3} . \tag{2}$$

Here $B_{\rm phot}$ is the magnetic field strength in the photosphere. In order to calculate $y_{\rm phot}$, we therefore only need to know the value of B in the photosphere and at some other height.

Assuming that the dipolar model describes the magnetic field gradient between the photosphere and the base of the transition region ($h \approx 2000$ km) and using the B values at $h = 0$ and 2000 km shown in Figure 14, we calculate dipole depths of $y_{\rm phot} = 9540$ km and 15,500 km for AR 7143 and AR 7150, respectively. These values can then be used in equation (2) to calculate the maximum dipolar field strengths $B_{\rm dip}$ at greater heights and in Figure 14 we plot the expected dipolar field strengths for the two active regions.

This figure shows that the maximum potential field is systematically higher than that expected for a dipole, with a larger discrepancy at greater heights. At $h = 20{,}000$ km, for example, we find $B_{\rm pot}/B_{\rm dip} = 1.5$ and 1.8 for AR 7150 and AR 7143, respectively. These results therefore suggest that if potential fields provide an accurate description of the magnetospheres of these regions, then they must diverge more slowly than expected from a simple dipole buried below the solar surface.

7. THEORETICAL MODELS FOR THE RADIO EMISSION ASSOCIATED WITH AR 7143 AND AR 7150

Recent comparisons of multiwavelength VLA observations of active regions with theoretical models of thermal gyroresonance radiation have been used to infer the heights of the sources and to constrain the temperature and density structure in the transition region and corona (Bogod et al. 1992). In this section we combine our potential field extrapolations with models of the electron temperature and density distribution to calculate the expected brightness temperature and circular polarization of the gyroresonance radiation associated with AR 7143 and AR 7150.

Theoretical maps of radio brightness temperature were produced by numerically solving the equation of radiative transfer along the line of sight over a 64 × 64 grid of positions enclosed by the magnetograms. Our calculations of optical depth, $\tau_{\rm gr}$, and brightness temperature, T_b, used the formulae given by Dulk (1985) and included contributions from the second, third,

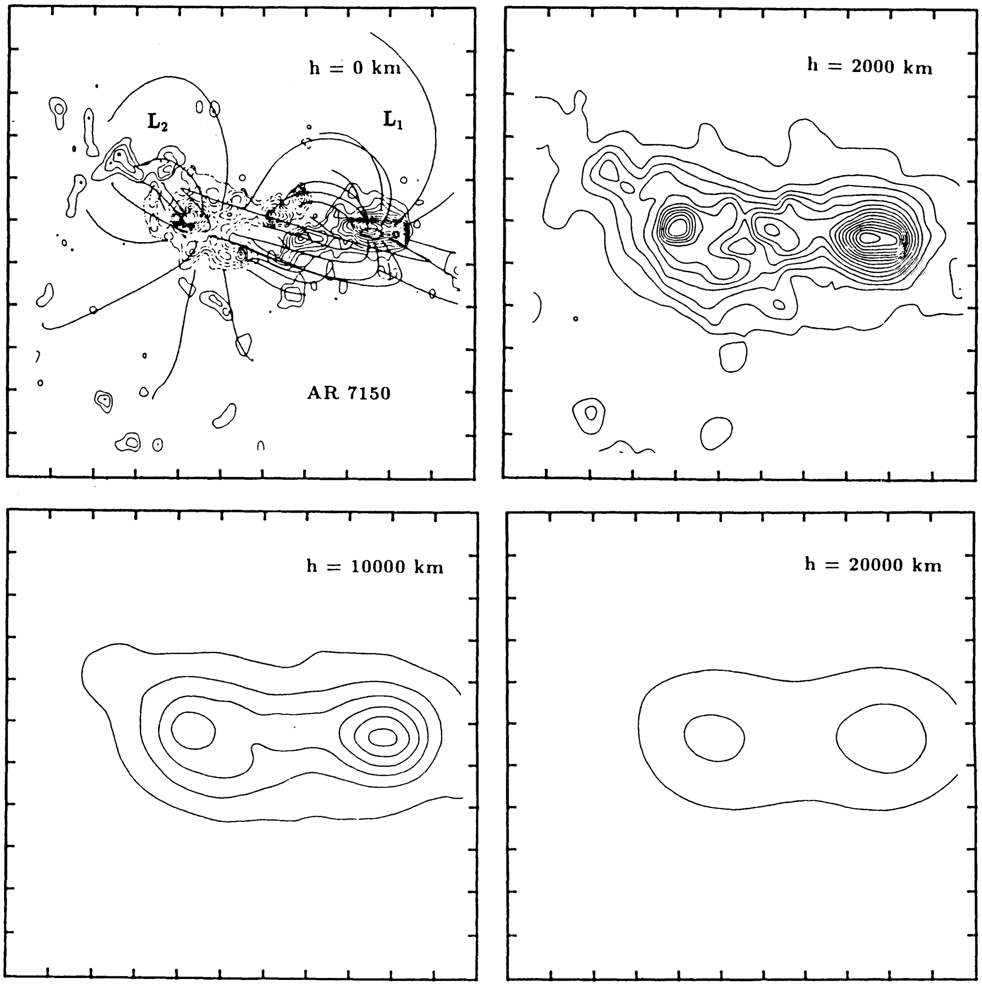

FIG. 13.—Contour maps showing total extrapolated magnetic field strengths at heights of 0, 2000, 10,000 and 20,000 km for AR 7150 on 1992 May 1. Extrapolated field lines are also shown superposed on the Kitt Peak magnetogram ($h = 0$ km). The outermost contour and contour interval of the Kitt Peak magnetogram is equal to 200 G; those for the extrapolated field maps are equal to 100 G. The angular scale may be inferred from the 30″ fiducial marks on the axes.

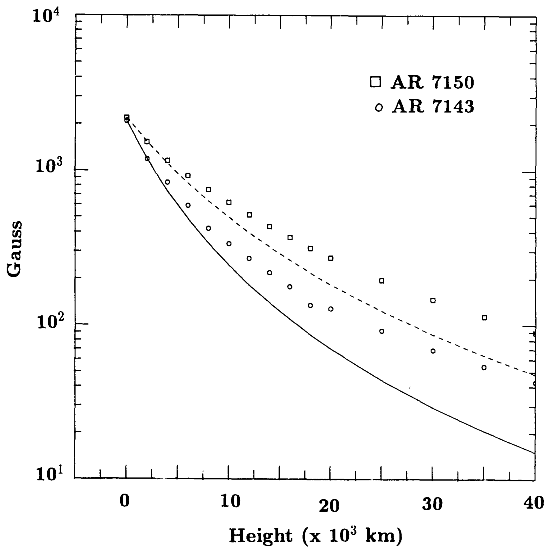

FIG. 14.—A plot of the maximum total magnetic field strength, $B_{\max}$, as a function of height above the solar surface. The dashed and solid lines show, respectively, the expected dipolar field strengths for AR 7150 and AR 7143.

and fourth harmonics of the gyrofrequency. The values of magnetic field strength in each thin ($\Delta h = 1000$ km) slice of the solar atmosphere were taken from the potential field maps at heights ranging between the transition region ($h = 2000$ km) to the low corona ($h = 40{,}000$ km). The gyroresonance parameters θ, the angle between the magnetic field and the line of sight, and $L_H = B/\nabla B$, the magnetic scale height, were obtained directly from the potential field extrapolations.

Two different types of models were considered for the distribution of T_e and N_e as a function of height in the transition region and corona. The first is the so-called conductive flux model, in which the conductive flux, F_c, is assumed to be constant between the base of the transition region and the corona. This model has been used by a number of investigators to compute the radio brightness temperature for a range of transition region thicknesses (e.g., Strong et al. 1984; Kruger, Hildebrandt, & Furstenburg 1985; Kruger & Hildebrandt 1985; Habbal et al. 1986). For this model the electron temperature as a function of height is given by (Alissandrakis, Kundu, & Lantos 1980)

$$T_e(h) = [(T_0^{7/2} + 3.5F_c(h - h_0)/A)]^{2/7} , \quad T_0 \leq T_e \leq T_c , \quad (3)$$

where T_0 is the temperature at the base of the transition region, T_c is the temperature of the corona, h is the height above the photosphere, h_0 is the height at which $T_e = T_0$, and A is a constant equal to 1.1×10^{-6} for F_c and h in cgs units. In our models, the corona is assumed to be isothermal with $T_c = 2 \times 10^6$ K.

Following Alissandrakis et al. (1980), we assume that the plasma above the active region is in hydrostatic equilibrium so that the gas pressure $P = N_e k T_e$ is

$$P = N_0 k T_0 \exp \left[-8.9 \times 10^{-11}(T_e^{5/2} - T_0^{5/2})/F_c\right] , \tag{4}$$

where N_0 is the electron density at the base of the transition region.

The second model for T_e and N_e is one developed by Rao & Kundu (1977) and Kundu, Melozzi, & Shevgaonkar (1986) in which the electron temperature is determined by a balance between thermal conduction and radiation losses. In this model the temperature and density gradients have an approximately power-law variation with height above the chromosphere so that they can be written as

$$\begin{aligned} T_e(h) &= T_0(h/h_{\min})^{\alpha} , \\ N_e(h) &= N_0(h/h_{\min})^{\beta} . \end{aligned} \tag{5}$$

Here α and β are power-law indices and $h_{\min}$ is a constant scale factor. If the gas pressure is assumed to be constant, i.e., $P = N_e k T_e =$ constant, it follows that $\beta = -\alpha$. This power-law model has been considered by Shevgaonkar & Kundu (1989) who found that it gave brightness temperatures that were consistent with VLA observations of active regions for the parameters $\alpha = -\beta = 0.7$ and $h_{\min} = 30$ km.

In our calculations, we assumed a transition region height of $h_0 = 2500$ km, a base temperature of $T_0 = 2 \times 10^4$ K, a base pressure of $P_0 = N_0 k T_0 = 2 \times 10^{15}$ cm^{-3} K, and a scale height of $h_{\min} = 30$ km. Theoretical maps of brightness temperature in both the ordinary and extraordinary modes of wave propagation were then computed for different values of the conductive flux ranging from $F_c = 2 \times 10^5$ to 1×10^7 ergs cm^{-3} s^{-1} and for values of the power-law index ranging from $\alpha = 0.7$ to 1.2.

In Table 5 we give values of the peak brightness temperature and circular polarization for different conductive flux and power-law models and in Figure 15 we show two-dimensional maps at 3.5, 6.2, and 20.7 cm for a particular conductive flux model ($F_c = 2 \times 10^6$ ergs cm^{-3} s^{-1}). The 6 cm maps shows compact sources ($T_b = 0.4$–1.4×10^6 K) which lie close to the underlying sunspots, in good agreement with the VLA map shown in Figure 9. The predicted 3.5 cm emission is confined to the region near the leading sunspot where the high magnetic fields make the source nearly optically thick. The 3.5 cm and 6.2 cm emission originates at the third harmonic at respective heights of $h \approx 4000$ km and $h \approx 10{,}000$ km. For $F_c = 2 \times 10^6$ ergs cm^{-3} s^{-1} these heights correspond to electron temperatures of $T_e = 1.0 \times 10^6$ K and 1.6×10^6 K and to electron densities of $N_e = 1.9 \times 10^9$ cm^{-3} and 1.0×10^9 cm^{-3}.

The computed 20 cm emission covers a much wider area due to the fact that lower magnetic fields ($B = 172$ G at the third harmonic) are required to make the source optically thick at this wavelength. Our calculations also indicate that any 2 cm gyroresonance emission would be optically thin and undetectable ($T_b \leq 10^4$ K) because the second and third harmonic layers ($B = 2678$ G and 1786 G) lie below the base of the model transition region. The bright looplike 2 cm source shown in Figure 9 is most likely produced by thermal bremsstrahlung (which is independent of B) from a dense structure in the transition region. Thermal bremsstrahlung probably also contributes to the 20 cm emission, especially in the "holes" or depressions above the sunspots where the vertical magnetic fields (corresponding to small θ) result in small optical depths and low brightness temperatures (see Dulk 1985).

Our models show that the observed peak brightness temperatures of $T_b = 8 \times 10^5$ K, 1.2×10^6 K, and 1.9×10^6 K at 3.5, 6.2, and 20.7 cm are consistent with conductive fluxes between $F_c = 2$–4×10^6 ergs cm^{-3} s^{-1}. Lower values of the F_c (corresponding to relatively thick transition regions) place the relevant third harmonic layers in regions of lower electron temperature resulting in lower brightness temperatures than are observed. Higher values of F_c produce the opposite effect at 3.5 and 6.2 cm. Similar conclusions were reached by Habbal et al. (1986) and Bogod et al. (1992) who compared theoretical models with VLA observations.

Our results also show that a power-law model with $\alpha = 0.7$, as used by Shevgaonkar & Kundu (1989), produces brightness temperatures that are significantly lower than observed. Increasing α to 1.2 increases the brightness temperature at 6.2 and 20 cm, but still yields an unacceptably low temperature ($T_b \approx 5 \times 10^5$ K) at 3.5 cm.

Although the conductive flux models give satisfactory results for AR 7150, models in which the corona is assumed to have a uniform temperature of $T_c = 2 \times 10^6$ K cannot explain the relatively high brightness temperatures of $T_b \approx 5 \times 10^6$ K in AR 7143. For a thermal plasma, the brightness temperature cannot exceed the electron temperature and if a higher coronal temperature of, say, $T_c = 5 \times 10^6$ K is assumed, then the gyroresonance emission at 6.2 and 20.7 cm will be optically thick with $T_b = T_c = 5 \times 10^6$ K. Since this is not observed, the high brightness temperature of the 3.5 cm emission must originate from a relatively thin, hot layer that is optically thick at the

TABLE 5

GYRORESONANCE MODEL CALCULATIONS FOR AR 7150

	CONDUCTIVE FLUX MODELS								POWER-LAW MODELS			
	$F_c = 5 \times 10^5$		$F_c = 2 \times 10^6$		$F_c = 5 \times 10^6$		$F_c = 1.0 \times 10^7$		$\alpha = 0.7$		$\alpha = 1.2$	
λ (cm)	T_{b_m} (K)	ρ_c (%)	T_{b_m} (K)	ρ_c (%)	T_{b_m} (K)	ρ_c (%)	T_{b_m} (K)	ρ_c (%)	T_{b_m} (K)	ρ_c (%)	T_{b_m} (K)	ρ_c (%)
2	$\leq 2 \times 10^4$	...	$\leq 2 \times 10^4$	...	$\leq 2 \times 10^4$	...	$\leq 2 \times 10^4$	...	$\leq 2 \times 10^4$	...	$\leq 2 \times 10^4$	...
3.5	3.4×10^5	86	5.6×10^5	80	7.7×10^5	75	9.7×10^5	70	2.4×10^4	90	4.8×10^5	87
6.2	9.9×10^5	8	1.4×10^6	10	1.9×10^5	8	2.0×10^6	0	4.1×10^5	7	2.0×10^6	0
20.7	1.4×10^6	5	2.0×10^6	0	2.0×10^6	0	2.0×10^6	0	9.3×10^5	30	2.0×10^6	0

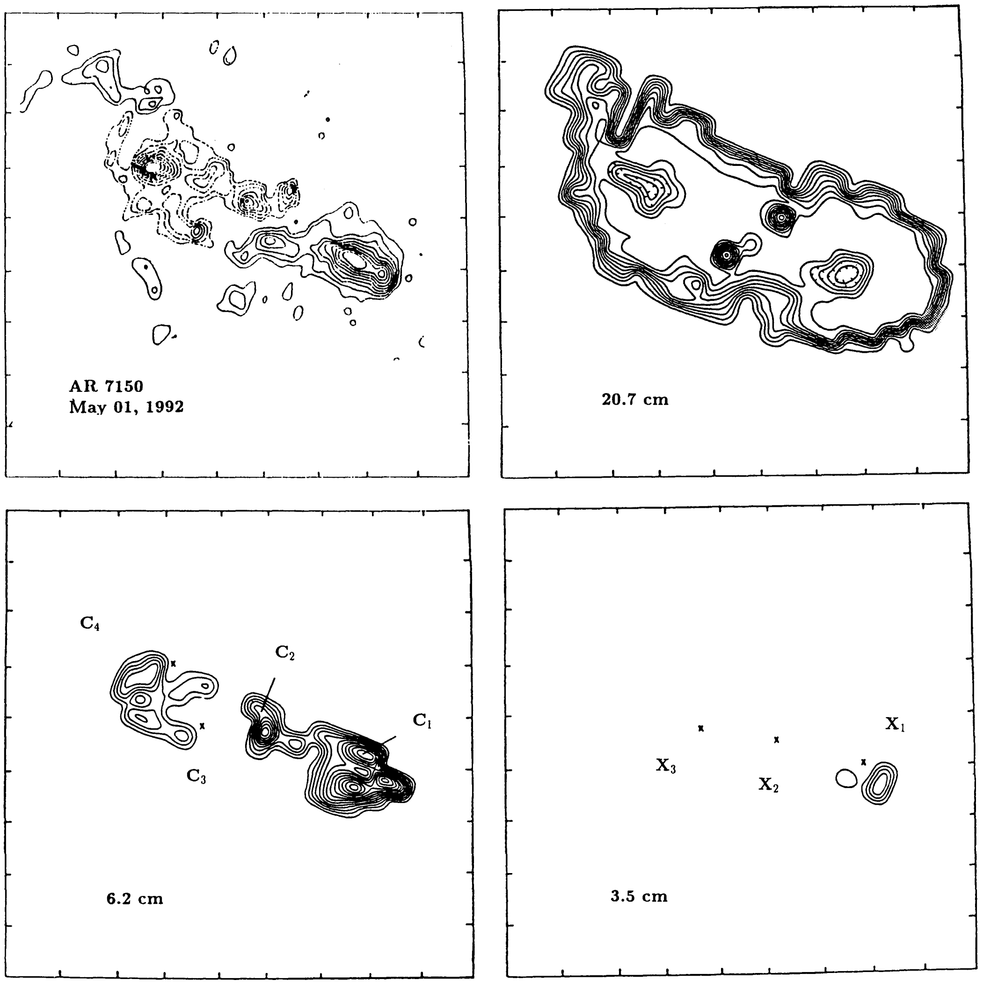

FIG. 15.—Predicted maps of thermal gyroresonance radiation at $\lambda = 3.5$, 6.2, and 20.7 cm for AR 7150 on 1992 May 1. Contours of photospheric magnetic field strength are also shown in the top left panel. The predicted maps were generated using the potential field extrapolations and a constant conductive flux of $F_c = 2 \times 10^6$ ergs cm^{-3} s^{-1}. The brightness temperature contours for each map are the same as those on the VLA maps shown in Fig. 8. The locations of the VLA sources X_1, X_2, X_3 and C_1, C_2, C_3, and C_4 seen in Fig. 9 at 3.5 and 6.2 cm, respectively, are also shown for comparison.

second or third harmonic. Such a hot, thin localized region may be confined within neutral current sheets in the corona, perhaps leading to long-lasting, nonthermal heating above the magnetic neutral line in the underlying photosphere.

We therefore modified our computer code to include a hot ($T_e = 5 \times 10^6$ K) localized region which coincides with the third harmonic gyroresonance layer at $\lambda = 3.5$ cm ($B = 1020$ G). For AR 7143 our potential field extrapolations indicate a height of $h = 3000$–4000 km for this layer. For $F_c = 2 \times 10^6$ ergs cm^{-3} s^{-1}, the 3.5 cm source has a peak brightness temperature of $T_b \approx 4.5 \times 10^6$ K, in good agreement with the observed value. The 6.2 and 20.7 cm sources have lower peak brightness temperatures ($T_b = 1.2 \times 10^6$ K and 1.9×10^6 K, respectively) because they originate at higher levels where the electron temperature assumes its normal coronal value of 2×10^6 K.

As suggested by Drago & Melozzi (1984) high brightness temperature sources might also be explained by the nonthermal gyrosynchrotron radiation of mildly relativistic electrons in coronal fields of ≈ 100 G. If this model is correct, then it should be able to account for the relatively narrow-band brightness spectrum which peaks at the short VLA wavelength of 3.5 cm. We therefore used the formulae given by Dulk (1985) to compute theoretical brightness temperature spectra of gyrosynchrotron radiation from a power-law distribution of electrons over the range of wavelength covered by the VLA. These formulae relate the optical depth, τ_{gs}, and the brightness temperature of gyrosynchrotron radiation to the energy spectral index, δ, the density of nonthermal electrons, N_{nt}, the path length through the source, L, the magnetic field strength in the source, B, and the angle between the line of sight and the magnetic field. In our calculations we assumed $N_{nt} = 10^{-3} N_e \approx 5 \times 10^6$ cm^{-3}, $L = 1.4 \times 10^9$ cm ($\theta_s = 10''$), and $\theta = 70°$. For an energy spectral index of $\delta = 3.5$ and $B = 100$ G, we find $T_{b_{gs}} = 5 \times 10^6$ K at 3.5 cm, but $T_{b_{gs}} = 4 \times 10^7$ K at 6.2 cm, a value that is nearly an order of magnitude greater than observed on May 1. Larger values of δ (e.g., $\delta = 5$–7) require higher values of B ($B = 460$–1200 G) in order to produce a brightness temperature of $T_{b_{gs}} = 5 \times 10^6$ K at 3.5 cm, but these models still predict unacceptably high brightness temperatures at 6.2 cm. Requiring that the nonthermal gyrosynchrotron source be optically thick at both 3.5 cm and 6.2 cm would result in lower brightness temperatures at 6.2 cm, but this constraint yields unacceptably high magnetic field

1993ApJ...419..398L

strengths of $B = 2.7 \times 10^5$ G to 8.2×10^3 G for $\delta = 3.5$–7. Given the fact that these models give results that are inconsistent with our data, we conclude that gyrosynchrotron radiation is probably not the explanation for the high brightness temperature source observed from AR 7143.

8. METHODS OF ENERGY RELEASE IN ACTIVE REGION MAGNETOSPHERES

The 1992 May data present a comparison of the magnetospheres of two active regions with dramatically different magnetic structures in the photosphere—a bipolar structure and a multipolar structure with a δ magnetic configuration. Although differences in magnetospheric structures may be partly due to the different stages in the history of development of the active regions (AR 7150 was near the maximum of its activity and AR 7143 in the decay stage), the main reason for the difference is most likely the magnetic configuration. Our analysis of the microwave emission from the decaying and smaller sunspot group AR 7143 suggests that the more intense emission at these wavelengths may be due to a hotter and relatively localized plasma embedded within a more homogeneous coronal structure. The idea that the high brightness temperature radio emission is due to the gyrosynchrotron radiation of nonthermal electrons is inconsistent with the lower brightness temperatures observed at longer wavelengths.

Roughly 20% of the large active region sources detected with the RATAN-600 are "peculiar" sources with a brightness temperature of $T_b \geq 10^7$ K, steep spectrum, low polarization ($\rho_c \approx 20\%$), and a position above the photospheric neutral line (see also Akhmedov et al. 1988). They are also associated with a multipolar δ configuration of the photospheric sunspots, and it is possible that all active regions with a multipolar δ-configuration and emerging photospheric flux will have associated peculiar sources of radio emission. However, the angular resolution of the RATAN-600 is not high enough to tell if active region structures smaller than 15″ are associated with peculiar sources. We point out that Correia, Kaufmann, & Strauss (1992) have also recently detected compact ($\theta \leq 1''$), high brightness temperature ($T_b = 2$–8×10^7 K) sources in nonflaring active regions at $\lambda = 1.3$ cm. These sources were also attributed to a hot plasma confined within neutral current sheets in the corona.

Although the peculiar source associated with AR 7143 is probably not due to gyrosynchrotron radiation, the hot, gyroresonance-emitting plasma may have been heated by nonthermal electrons. The nonthermal electrons were probably accelerated by magnetic reconnection in the complex magnetosphere of AR 7143 and are now localized within neutral current sheets by the magnetic pressure of the surrounding corona.

9. CONCLUSIONS

The detailed spectral polarization observations of the RATAN-600 and the high spatial resolution observations of the VLA have been used to infer the physical parameters and radiation mechanisms of a number of quiescent active region structures. Our most significant results may be summarized as follows.

1. The RATAN spectral observations have been combined with the theory of cyclotron emission to show that the magnetic field strengths in the corona above large sunspots is often 75–80% of the magnetic field strength in the underlying sunspots.
2. VLA observations of coronal loops at 20 cm wavelength have been compared with soft X-ray images from the *Yohkoh* satellite to show that the bright radio and X-ray structures coincide, but that there is also radio emission that is not detectable at X-ray wavelengths. Variable soft X-ray emission on timescales of hours suggests some sort of continued, varying low-level heating or particle acceleration in localized areas of active regions.
3. Coronal potential field extrapolations indicate vertical magnetic field gradients of $\Delta B/\Delta h \approx -0.2$ G km^{-1} for the bipolar active region AR 7150 and $\Delta B/\Delta h \approx -0.3$ G km^{-1} for the multipolar region AR 7143. These gradients are comparable to those obtained from magnetic field extrapolations by other investigations, while also suggesting that the coronal fields diverge more slowly than expected for a dipole located below the solar surface.
4. Comparisons of theoretical models with multiwavelength VLA images and potential field extrapolations indicate that the microwave emission from AR 7150 can be largely explained as third harmonic thermal gyroresonance radiation in a conductive flux model. Our results constrain the conductive flux in such models to the range $F_c = 2$–4×10^6 ergs cm^{-3} K^{-1}. In contrast, the high brightness temperature and steep radio spectrum for AR 7143 cannot be explained by conventional thermal models. Instead it suggests long-lasting nonthermal heating in localized coronal sources along the magnetic neutral line above the photosphere. Gyrosynchrotron radiation of nonthermal electrons cannot explain the observations of this source, but heating within a localized neutral current sheet might account for them.
5. Long-lasting radio sources with high brightness temperatures $\geq 10^7$ K and steep radiation spectra are often associated with active regions with a multipolar δ configuration of the photospheric sunspots. These "peculiar" coronal radio sources appear above the neutral line in the photosphere, and appear to require nearly continuous acceleration of energetic nonthermal electrons by a yet unknown process. The complicated multipolar structure of the active region's magnetic fields is, in fact, consistent with the presence of current sheets, nonthermal heating, and high brightness temperature sources.

Collaborative VLA-RATAN observations of the Sun at Tufts University are supported by Collaborative Research Grant 921394 of the North Atlantic Treaty Organization (NATO) and by the US-USSR Cooperative Research Program of the National Science Foundation under grant ATM 9024506. Radio astronomical studies of the Sun at Tufts University are also supported by NASA grant NAGW-2383. The VLA is operated by Associated Universities, Inc., under contract with the National Science Foundation. The *Yohkoh* SXT operations and analysis are supported under grant NAS8-37334 and by the Lockheed Independent Research Program.

REFERENCES

Abramov-Maximov, V. E., & Gelfreikh, G. B. 1983, Pisma Astron. Zh., 9, 244
Akhmedov, Sh. B., et al. 1986, ApJ, 301, 460
Akhmedov, Sh. B., Gelfreikh, G. B., Bogod, V. M., & Korzhavin, A. N. 1982, Sol. Phys., 79, 41
Alissandrakis, C. E., Kundu, M. R., & Lantos, P. 1980, A&A, 82, 30
Bogod, V. M., Vyalshin, G. F., Gelfreikh, G. B., & Petrova, N. S. 1982, Soln. Dannye, No. 1, 104
Bogod, V. M., Gelfreikh, G. B., Willson, R. F., Lang, K. R., Shatilov, V., & Tsvetkov, S. V. 1992, Sol. Phys., 141, 303
Bogod, V. M., Vatrushin, S. M., Abramov-Maximov, V. E., Tsvetkov, S. V., & Dikij, V. N. 1993, in IAU Colloq. 141, in press
Brosius, J. W., & Holman, G. D. 1988, ApJ, 342, 1172
Brosius, J. W., Willson, R. F., Holman, G. D., & Schmelz, J. T. 1992, ApJ, 386, 347
Correia, E., Kaufmann, P., & Straus, F. M. 1992, Sol. Phys., 138, 223
Drago, F. C., & Melozzi, M. 1984, A&A, 131, 103
Dulk, G. A. 1985, ARA&A, 23, 169
Habbal, S. R., Ronan, R. S., Withbroe, G. L., Shevgaonkar, R. K., & Kundu, M. R. 1986, ApJ, 306, 740
Hara, H., Tsuneta, S., Lemen, J. R., Acton, L. W., Mctiernan, J. M. 1992, PASJ, 44, L135
Khaikin, S. E., Kaidanovskii, N. L., Parijskij, Yu, N., & Esepkina, N. A. 1972, Isvestia Main Astron. Obs. Pulkova, 188, 3
Kruger, A., & Hildebrandt, J. 1985, Astron. Nach., 306, 157
Kruger, A., Hildebrandt, J., & Furstenburg, F. 1985, A&A, 143, 72
Kundu, M. R., Melozzi, M., & Shevgaonkar, R. K. 1986, A&A, 167, 166
Lang, K. R., Willson, R. F., Bogod, V. M., and Gelfreikh, G. B. 1993, ApJ, submitted
Lang, K. R., Willson, R. F., Smith, K. L., & Strong, K. T. 1987a, ApJ, 322, 1035
———. 1987b, ApJ, 322, 1044
Parijskij, Yu. N., et al. 1976, Sov. Astron., 20, 577
Rao, A. P., & Kundu, M. R. 1977, Sol, Phys., 55, 161
Sakurai, T. 1982, Sol. Phys., 76, 301
Sakurai, T., & Uchida, Y. 1977, Sol. Phys., 52, 397
Shevgaonkar, R. K., & Kundu, M. R. 1984, ApJ, 283, 413
———. 1989, ApJ, 342, 586
Strong, K. T., Alissandrakis, C. E., & Kundu, M. R. 1984, ApJ, 277, 865
Tsuneta, S., et al. 1991, Sol. Phys., 136, 37
White, S. M., Kundu, M. R., & Gopalswamy, N. 1991, ApJ, 366, L43